Single-molecule optical microscopy of protein dynamics and computational analysis of images to determine cell structure development in differentiating *Bacillus subtilis*

Adam J. M. Wollman[a], Katarína Muchová[b], Zuzana Chromiková[b], Anthony J. Wilkinson[c,], Imrich Barák[b,], Mark C. Leake [a,*]

[a] Departments of Physics and Biology, University of York, York YO10 5DD, United Kingdom.

[b] Institute of Molecular Biology, Slovak Academy of Sciences, Bratislava, Slovakia.

[c] Structural Biology Laboratory, Department of Chemistry, University of York, York, YO10 5DD, United Kingdom.

[*] Email: mark.leake@york.ac.uk

Abstract

Here we use singe-molecule optical proteomics and computational analysis of live cell bacterial images, using millisecond super-resolved tracking and quantification of fluorescently labelled protein SpoIIE in single live *Bacillus subtilis* bacteria to understand its crucial role in cell development. Asymmetric cell division during sporulation in *Bacillus subtilis* presents a model system for studying cell development. SpoIIE is a key integral membrane protein phosphatase that couples morphological development to differential gene expression. However, the basic mechanisms behind its operation remain unclear due to limitations of traditional tools and technologies. We instead used advanced single-molecule imaging of fluorescently tagged SpoIIE in real time on living cells to reveal vital changes to the patterns of expression, localization, mobility and stoichiometry as cells undergo asymmetric cell division then engulfment of the smaller forespore by the larger mother cell. We find, unexpectedly, that SpoIIE forms tetramers capable of cell- and stage-dependent clustering, its copy number rising to ~700 molecules as sporulation progresses. We observed that slow moving SpoIIE clusters initially located at septa are released as mobile clusters at the forespore pole as phosphatase activity is manifested and compartment-specific RNA polymerase sigma factor, σ^F, becomes active. Our findings reveal that information captured in its quaternary organization enables one protein to perform multiple functions, extending an important paradigm for regulatory proteins in cells. Our findings more generally demonstrate the utility of rapid live cell single-molecule optical proteomics for enabling mechanistic insight into the complex processes of cell development during the cell cycle.

Keywords: Single-molecule, sporulation, super-resolution, morphogenesis, differentiation.

1. Introduction

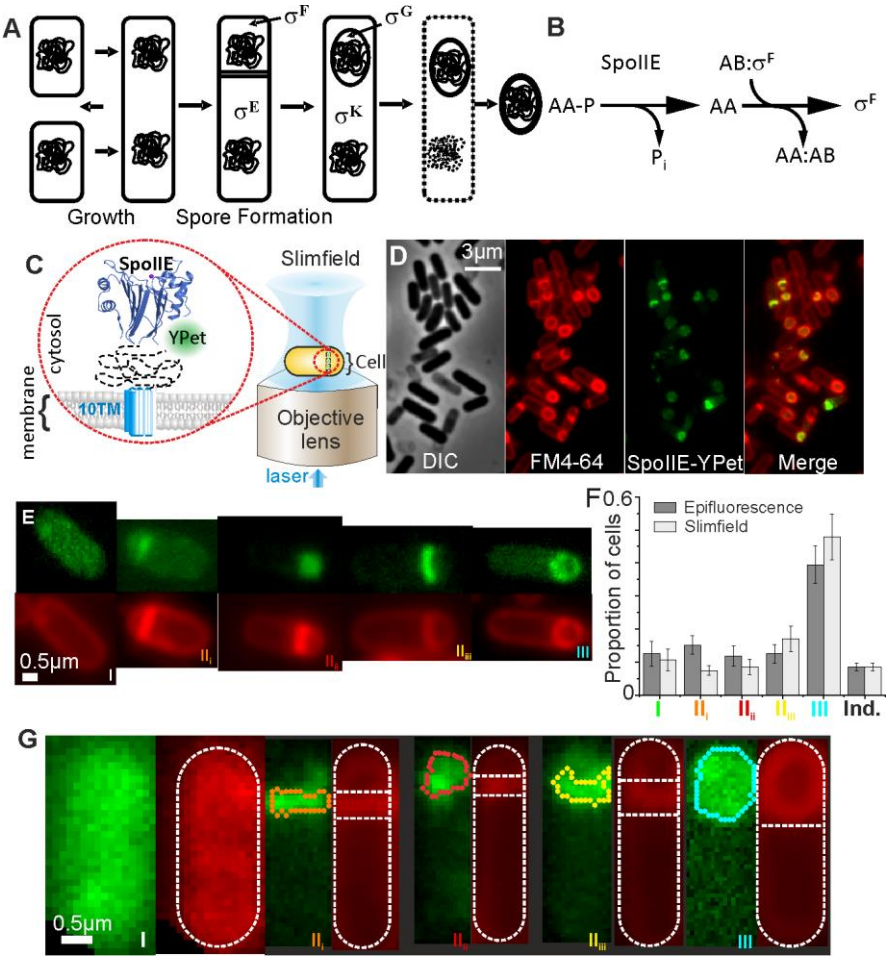

Figure 1: Fluorescence imaging and classification by sporulation stage (A) Growth and sporulation of *B. subitlis*. During spore formation, the cell divides asymmetrically producing a smaller forespore and a larger mother cell. Compartment and stage specific sigma factors are activated sequentially. The forespore is engulfed by the mother cell before maturing into a resistant spore which is released when the mother cell lyses. (B) The SpoIIE phosphatase is the most upstream-acting of three proteins regulating the activity of the first compartment-specific sigma factor, σ^F. Dephosphorylation allows SpoIIAA (AA) to displace σ^F from its complex with an anti-sigma factor (AB) enabling forespore-specific gene expression to be established. (C) Slimfield schematic, inset showing septum-localised SpoIIE-mYPet. (D)

phase/epifluorescence microscopy of SpoIIE at different stages. Membrane labelling, FM4-64 (red), SpoIIE-mYPet (green). (E) **Example epifluorescence images of SpoIIE-mYPet (green) with membraned stained with FM4-64 (red) at each stage.** (F) Detected mean proportion of each stage or indeterminate (Ind.) (SEM error) of N = 4 fields of view each containing approximately N =100 cells. Proportions were statistically identical between epifluorescence and slimfield data at p=0.05 (p=0.40,0.08, 0.29, 0.72, 0.72,0.49 for each stage/indeterminate respectively) (G) Categorization of stages from Slimfield, detected forespore/septa features (coloured lines), cell boundary segmentation based on fitting a sausage shape to fluorescence image indicated (outer white dash) and interface between forespore, septa and mother cell (horizontal white dash).

Spore formation in *B. subtilis* offers a model system for studying development, differentiation, morphogenesis, gene expression and intercellular signalling in complex organisms[1,2]. In nutrient rich conditions, rod-shaped cells grow and multiply by symmetric mid-cell division to generate identical daughters (Fig. 1A). However, when starved, *B. subtilis* ceases growth and is able to embark on a pathway of differentiation to form a dormant cell called a spore. Spore formation begins with an asymmetric division producing a smaller forespore cell next to a larger mother cell. Each compartment inherits an identical chromosome, but the patterns of gene expression, orchestrated by compartment-specific RNA polymerase sigma factors, differ resulting in alternative cell fates. The mother cell engulfs the forespore in a phagocytosis-like process creating a cell-within-a-cell (Fig. 1A), and a nurturing environment in which a robust multi-layered coat is assembled around the maturing spore[3]. In the final stages, the mother cell undergoes programmed cell death releasing the spore, which is resistant to multiple environmental stresses and can lie dormant until favourable growth conditions are restored.

At sporulation onset, ring-like structures of the tubulin homologue FtsZ form at mid-cell and migrate on diverging spiral trajectories towards the cell poles[4], colocalizing with the membrane integrated phosphatase PP2C SpoIIE[5]. One polar ring matures into the sporulation septum while the other disassembles[6]. Asymmetric division otherwise involves the same proteins as vegetative cell division, though the resulting sporulation septum is thinner[7,8]. SpoIIE is the only sporulation-specific protein whose mutation causes ultrastructural changes in the asymmetric septum; null mutants of *spoIIE* are defective in sporulation and at lower frequency give rise to thicker asymmetric septa resembling the vegetative septum[7].

Changes in cell morphology during sporulation are coupled to a programme of gene expression, involving intercellular signalling, and the sequential activation of RNA polymerase sigma factors, σ^F and σ^G in the forespore and σ^E and σ^K in the mother cell[9]. Forespore-specific activation of σ^F on completion of the asymmetric septum is the defining step in differentiation. In pre-divisional and mother cells, σ^F resides in complex with the anti-sigma factor SpoIIAB while a third protein SpoIIAA is phosphorylated. After septation, SpoIIAA~P is dephosphorylated by the manganese-dependent protein phosphatase SpoIIE. The resulting SpoIIAA displaces σ^F from the σ^F:SpoIIAB complex allowing RNA polymerase binding and transcription of forespore-specific genes (Fig. 1B)[10,11]. This in turn, triggers activation of σ^E in the mother cell and establishes alternate programmes of gene expression which determine different cell fates (Fig. 1A).

SpoIIE has multiple roles at different sporulation stages (Fig. 1A,B). Assembly of SpoIIE to form polar rings – "E-rings", dependent on interaction with FtsZ[12], occurs during stage I, defined by the formation of an axial filament spanning the cell length and comprising two copies of the chromosome each tethered through its origin region to opposing cell poles. Formation of the asymmetric septum is defined as stage II_i, during which SpoIIE interacts with the divisome components RodZ[13] and DivIVA[14]. After closure of the sporulation

septum, the FtsZ ring disassembles. SpoIIE-mediated activation of σ^F correlates with release of SpoIIE from the sporulation septum, marking stage II_{ii}[13]. During stage II_{iii}, SpoIIE interacts with SpoIIQ[15] the forespore component of an intercellular channel[16–18], crucial for later activation of σ^G. Stage III is characterized by mother cell engulfment of the forespore; SpoIIE localizes around the forespore, but there are no data to suggest a specific role of SpoIIE in this or later stages[15].

An increased concentration of SpoIIE in the forespore relative to that in the mother cell has been proposed to account for the selective activation of σ^F in the emerging forespore. This may occur through equipartitioning SpoIIE into the mother cell and forespore septal membranes leading to a higher SpoIIE effective concentration in the forespore as a result of its ~6 fold smaller volume [19]. It has also been shown that there is selective proteolysis of SpoIIE in the mother cell through the action of the membrane bound ATP-dependent protease, FtsH[20]. Here, it is proposed selective oligomerization at the forespore pole, protects SpoIIE from proteolysis in this compartment and further increases the concentration difference between the cell compartments.

To explore the complex function of SpoIIE further, we sought to determine its dynamic molecular architecture in differentiating cells. We employ a rapid single-molecule optical proteomics technique Slimfield imaging[21–23] capable of tracking single fluorescently-labelled SpoIIE molecules with millisecond sampling in live *B. subtilis* cells to super-resolved spatial precision. By using step-wise photobleaching of the fluorescent protein tags[24] we determine the stoichiometry of each tracked SpoIIE complex and quantify the precise number of SpoIIE molecules in the mother cell and forespore in each individual cell . Also, by analysing the mobility of SpoIIE foci via their mean square displacement with respect to time, we calculate the microscopic diffusion coefficient *D*, model this to determine the effective diameter of SpoIIE complexes and correlate these data with measured SpoIIE

content. Importantly, our copy number estimates indicate that there are similar numbers of SpoIIE molecules in both the mother cell and the forespore compartments when the asymmetric septum forms: since the volume in the forespore is significantly smaller than that of the mother cell this finding reveals an order of magnitude higher SpoIIE concentration in the forespore, correlated to the increased activity of σ^F. We find that the stoichiometry and diffusion of tracked SpoIIE is dependent on its interaction partners and morphological changes, suggesting its roles in sporulation are influenced by oligomeric composition and mobility. Interestingly, we detect higher order mobile, oligomeric SpoIIE, towards the cell pole, at the stage of sporulation when σ^F becomes selectively activated in the forespore, as previously proposed[20].

2. Methods

2.1 Strains and plasmids

Gene cloning in *B. subtilis*, unless specified, was performed using standard protocols[25] (Table S1). To construct pSGIIE-mGFP, used in the FRAP experiments, we used previously prepared pSGIIE-YPet[13]. A PCR fragment containing mGFP was prepared using mGFPKpnF:

5’ ATCATCATCGGTACCATGAGTAAAGGAGAAGAACTTTTCACTGGAGTTGTC 3’

and mGFPBamR2:

5’ atcatcatcggatccTTATTTGTATAGTTCATCCATGCCATGTG 3’

primers and a plasmid derivative pSG1729 containing *mgfp* as template[26]. To yield pSG-mGFP this fragment was KpnI/BamHI digested and cloned into a similarly cut pSGIIE-YPet. Subsequently a 360bp KpnI fragment containing *spoIIE* C-terminus (obtained from

KpnI/BamHI cut pSGIIE-YPet) was cloned into pSG-mGFP digested with KpnI to yield pSGIIE-mGFP.

B. subtilis liquid cultures were grown in DSM [25] supplemented with chloramphenicol (5μg ml^{-1}), erythromycin (1μg ml^{-1}) and lincomycin (25μg ml^{-1}) as required. Samples for microscopy on 1% agarose slides were taken 2h after sporulation onset (from our measurements this would ensure that the majority of cells after the onset of sporulation would have reached the start of stage II). For membrane visualization, FM 4–64 (Molecular Probes) was used (0.2–1μg ml^{-1}). When necessary, cells were concentrated by centrifugation (3min, 2,300 x g) and resuspended in a small volume of supernatant. Images and analysis were obtained with an Olympus BX63 microscope (Hamamatsu Orca-R^2 camera) and Olympus CellP or Olympus Image-Pro Plus 6.0 software. Imaging was performed at room temperature.

As N-terminal, cytosolic tail of SpoIIE (residues 11 to 37) is responsible for its proteolysis by FtsH (20), it is not possible to determine by western blot if the protein was degraded due to the fluorescent tag (Fig. S1C). It is also impossible to select only early stage sporulating cells corresponding to our microscopy data in western analysis as the fusion protein construct SpoIIE-mYPet localizes to the membrane and the cells sporulate at the level of the wild type cells, we believe the fusion protein is expressed, is functional and is degraded as the untagged version. Also, we did not detect any cytoplasmic fluorescence consistent with cleaved fluorescent protein alone (background fluorescence was consistent with out of plane foci – see later section). Epifluorescence images showed integration into the membrane (Fig. S1A)

and simulated images of membrane integrated SpoIIE were qualitatively the same as our Slimfield images (Fig. S1B).

2.2 Single-molecule optical proteomics

A dual-color bespoke single-molecule microscope was used as described previously [23,27] which utilized narrow epifluorescence excitation of 10 μm full width at half maximum in the sample plane from a 514 nm 20mW laser (Obis LS, Coherent). The laser was propagated through a ~3x Keplerian beam de-expander. Illumination was directed onto an *xyz* nanostage (Mad City Labs, the Dane County, Wisconsin, USA), and emissions directed through a color splitter utilizing a dichroic mirror centered on 560 nm wavelength and emission 25nm bandwidth filters centered at 542/594 nm (Chroma Technology Corp., Rockingham, Vermont, USA) onto an Andor iXon 128 emCCD camera, 80 nm/pixel. Brightfield imaging was performed with no gain (100 ms/frame), single-molecule imaging at maximum gain (5 ms/frame).

Foci were automatically detected using MATLAB (Mathworks) software enabling a spatial localization precision of 40nm using iterative Gaussian masking, and automated *D* and stoichiometry calculation. The copy number in the mother cell or forespore was determined by summing pixel intensities within the compartment, correcting for low background autofluorescence measured from FM4-64 labeled wild type *B. subtilis*, then dividing by the characteristic SpoIIE-mYPet intensity [27]. The intensity of each foci was defined as the summed intensity inside a 5 pixel radius circle corrected for the local background, defined as the mean intensity in a 17 pixel square outside the circle [24]. If the signal to noise ratio of the foci, defined as the mean intensity divided by the standard deviation of the local background, was greater than 0.4 it was linked into an existing track if within 5 pixels, approximately matching the diffraction-limited point spread function width. Only tracks with 4 or more points were analyzed, a commonly used criterion by us and others in the single-

particle tracking field[28,29]. The characteristic SpoIIE-mYPet intensity was calculated from foci intensities found towards the end of the photobleach, confirmed to be single molecule from detection of single step-wise photobleach events in individual over-tracked (i.e. tracked beyond photobleaching), Chung-Kennedy[30] filtered (an edge preserving smoothing algorithm) SpoIIE-mYPet tracks (Fig. S2). The stoichiometry of tracked foci was determined by fitting the first 4 intensity values of each track with exponential:

$$\boldsymbol{I = I_0 \exp(-\frac{t}{t_b})}$$

I = foci intensity, I_0= initial intensity, t = time since laser illuminated cell, t_b=bleach time (determined by an exponential fit to all population foci intensity to be ~100ms). I_o was divided by the mYPet characteristic intensity to give the stoichiometry. Although sub-optimal for low stoichiometry foci, e.g. <6 molecules per focus, this exponential method is effective over a broad range of stoichiometries[31]

The 2D mean square displacement (MSD) was calculated from a fitted foci centroid $(x(t),y(t))$ assuming a track of N consecutive frames, and a time interval $\tau = n\Delta t$, where n is a positive integer and Δt the frame integration time [32]:

$$MSD(\tau) = MSD(n\Delta t) = \frac{1}{N-1-n}\sum_{i=1}^{N-1-n}\left\{\left[x(i\Delta t + n\Delta t) - x(i\Delta t)\right]^2 + \left[y(i\Delta t + n\Delta t) - y(i\Delta t)\right]^2\right\}$$
$$= 4D\tau + 4\sigma^2$$

The localization precision from tracking is given by σ, which we measure as 40nm. D is estimated from a linear fit to the first three data points in the MSD *vs*. τ relation (i.e. $1 \le n \le 3$) for each accepted track, with the fit constrained to pass through a point $4\sigma^2$ on the vertical axis corresponding to $\tau = 0$, allowing σ to vary in the range 20 - 60nm in line with the experimental range.

2.3 FRAP

FRAP was carried out on a Zeiss LSM 510 Meta confocal system with Axiovert inverted microscope, fitted with Plan Apochromat 100x /1.4 NA oil objective and temperature-controlled stage. A 488nm wavelength laser excited GFP, emissions collected via a 498-564nm bandpass filter. The strength of photobleaching in the region of interest was set to 10-20 iterations of 100ms each to ensure maximal photobleaching of GFP inside and minimum photobleaching beyond.

2.4 Categorization of cell cycle stage

To determine the cell cycle stage during the sporulation process, the following algorithm was used:

1. Cell images were initially coarsely over-segmented by thresholding the brightfield image and then using an initial ellipse shape approximation to define the cell length [27]. We then manually optimised the cell width of a sausage function (rectangle capped with two hemicircles) that enclosed the mYPet fluorescence intensity in each cell above the level of background noise.
2. Cells were then cropped out of the original image using a bounding rectangle around the segmentation and automatically rotated parallel to the horizontal axis.
3. A more precise segmentation stage then followed. This consisted of a double threshold Otsu's method, applied to a 5 frame average of the mYPet fluorescence image. Pixels whose intensity values were above the 2nd threshold and multiplied by the segmentation contain the spore feature – either the whole forespore or septa.
4. These pixel areas were split into distinct connected components or candidate spore features and their centroids and areas calculated automatically using standard MATLAB functions.
5. A region was accepted as the mYPet spore feature mask if:

1. Its centroid is within 40% of either end of the cell.
2. Its centroid is within ±40% of the middle of the cell width.
3. The area of its centroid was >10 pixels (there was no upper threshold).
4. It had the highest summed pixel intensity of all the regions.

6. If nothing was accepted, steps 5.1-5.4 were repeated once with the previously found regions excluded.
7. If nothing was still found then the cell is 'pre-sporulation/stage I'.
8. The FM4-64 frame average was similarly segmented but the mask multiplied by the forespore mask to give the FM spore feature.
9. Both FM and mYPet spore feature Major/Minor Axis, Area and Orientation were calculated by fitting the shape to an ellipse function.
10. Both were then assigned into 2 shape categories based on the aspect ratio, > 1.2 – 'septa', otherwise 'filled' structure. These correspond to fluorescence only at the linearly extended septa or distributed about the forespore in a rounder shape.
11. If the FM segmentation was 'septa', the segmentation was morphologically 'thinned' and its linear curvature calculated.
12. Stages were then assigned as follows:

Stage I/pre-sporulation: no mYPet spore feature detected.

Stage II_i: 'septa' FM and mYPet spore features with curvature <1.

Stage II_{ii}: 'septa' FM and 'filled' mYPet spore features.

Stage II_{iii}: 'septa' FM and mYPet spore features with curvature >1.

Stage III: 'filled' FM and mYPet spore features.

To confirm the spore categorization algorithm we tested it on a series of simulated images (Fig S1C). These were generated by integrating a model point spread function (PSF) over a

3D model for the cell and forespore shape and subsequently noising the image with Poisson noise based on real noise characteristics of our microscope [33]. The cell membrane was modelled as a hollow cylinder, capped with hemisphere shells at either end with 1 pixel thick walls. Stage II_i septa were modelled as cell width disks while stage II_{iii} septa were modelled as hemispherical shells. Released SpoIIE in stage II_{ii} was modelled as a hemispherical shell capped by a disk while in stage III, it was modelled as a spherical shell. The relevant features for 100 cells in each stage were simulated in the 'mYPet' and 'FM4-64' channels and run through the categorization algorithm as if they were real data with no noise, average noise and the most extreme noise observed in the data. Without noise. 100% of cells were correctly identified, dropping to at worst in stage II_{ii} 79% with average noise and in the extreme case, as low as 42%.

We attempted further confirmation using Principal Component Analysis (PCA), an approach typically used to identify specific conformations or orientations in cryo-electron microscopy data. Data, images in this case, can be broken down into a basis set of eigenvectors or eigenimages which when summed in proportion to their eigenvalues, recreate the original dataset. Its use in live cell fluorescence data is challenging due to the high heterogeneity in size, shape and intensity of the images. Thus spore images were all cropped to 16x16 pixels, rotated and aligned and their intensity normalised (Fig. S1H) before a basis set of eigenvectors were calculated by Hotelling's deflation [34]. The distribution of eigenvalues was strongly biased towards the 1st eigenvector (Fig. S1I) however 3D scatter plots of the first 3 eigenvalues did show separation of the data, further confirming our categorization algorithm but not allowing us to categorise spores based on PCA alone.

2.5 Determining the contribution from out-of-focus SpoIIE-mYPet foci

To quantify the contribution from out-of-focus SpoIIE-mYPet foci (i.e. those not detected during tracking) into the membrane 'pool' (i.e. spatially extended membranous regions of

fluorescence intensity not detected as distinct foci), we assumed that the number and stoichiometry of detected foci from within the depth of field were the same as those without and were uniformly distributed. Assuming a depth of field of ~350nm, on the basis of expectations from the numerical aperture of the objective lens and peak emission wavelength, a mean cell width of ~0.9 µm (61) and that the focal plane is exactly on the cell midplane we estimate ~1/4 of the cell membrane lies in the depth of field of the microscope. Thus, to generate indicative estimates for copy number values per cell we extrapolated the total number of summed SpoIIE-mYPet in foci by a factor of 4x. For the stage II mother cell (Table S2), the mean total number of molecules in foci per cell is ~32 (Mean foci stoichiometry multiplied by mean number of foci per cell) which multiplied by 4 agrees with the mean copy number of 82±42 to within experimental error. Using the same method on other stages either agrees or over or underestimates implying that there is no measurable 'pool' of SpoIIE i.e. all of the SpoIIE-mYPet fluorescence can be accounted for by foci.

2.6 Simulating the effects of different oligomeric states for SpoIIE on the predicted stoichiometry distribution from Slimfield analysis

To simulate the effects of different oligomeric states of SpoIIE-mYPet on the observed stoichiometry distribution from Slimfield image data we calculated the probability of foci overlap[36] in each individual cell using the number of detected foci and the area of the spore feature in that particular cell. This probability was used to generate the distribution of overlaps using a Poisson distribution, based on a stage specific frequency of overlap, λ. The predicted apparent stoichiometry distribution was then generated by convolving the overlap distribution with the intensity distribution of model stoichiometry, S (i.e. S = 2, dimers, S = 4, tetramers etc.). This intensity distribution was generated from the mYPet characteristic intensity distribution (Fig. S2C), re-centred on 2S, width scaled to $S^{1/2}$*σ, where σ = 0.675,

the sigma width of Fig. S2C. Such that the probability distribution of stoichiometries $P(x)$ is given by:

$$P(x) = \sum_{k=1}^{5} \exp(-\lambda) \frac{\lambda^k}{k!} \frac{1}{\sigma\sqrt{2\pi kS}} \exp(-\frac{x - kS}{k\sigma^2})$$

This model is a summation of multiple Gaussian distributions which are separated by a fixed number of molecules (for example 4 molecules in the case of the tetramer model), whose amplitude scales with a Poisson distribution, as expected from the nearest neighbour model. Here k is the number of overlapping foci – we sum up to a maximum of $k = 5$ overlapping foci since this ensured in all cases that the expectation value of foci occurrence at higher values of k was less than 1 (i.e. $P.S<1$ focus). Finally, each of these modelled cell stoichiometry distributions was averaged over the sporulation stage population to generate the model distribution and convolved with the same 0.7 molecule width kernel as the kernel density estimates (KDEs) in the real (i.e. experimental) data. The Pearson's Chi-squared statistic χ^2 was calculated as:

$$\chi^2 = \sum_{i=1}^{30} \frac{(O_i - C_i)^2}{C_i}$$

where the observed value O_i is the normalized KDE value (i.e. scaled on the probability density axis such that the total area underneath the KDE sums exactly to 1) at single molecule bin intervals up to a total of typically $n = 30$ bins, i.e. stoichiometry range tested from the full distribution is 0-30 molecules, assuming the data contained at least one recorded focus in any respective bin (if not it was discarded in the Chi-squared summation). The calculated data value C_i was taken from the normalized model fit. The degrees of freedom were equal to the number of bins used in the χ^2 calculation subtracting the 4 free model parameters (which were overlap frequency (λ), max number of overlaps (k), intensity distribution (σ) and model stoichiometry (S)). The value of the measured χ^2 was then used with the inbuilt inverse Chi-

squared MATLAB function chi2cdf.m at this equivalent number of degrees of freedom to calculate the equivalent p value which corresponds to the null hypothesis that the measured variation between the observed values and the model fit is random. We found that the tetramer model was the only model to produce a goodness of fit corresponding to acceptable p values at approximately 0.05 or less in all stages (Fig. 3 and S3).

2.7 Modelling the frictional drag on SpoIIE foci

We modelled the frictional drag coefficient in the cell membrane of SpoIIE foci as that due to a cylinder whose height h matches the width of the phospholipid bilayer (~3nm) with a radius given by parameter a, using a generalized method established previously to characterize the lateral diffusion of transmembrane proteins [37,38]. In brief, the diffusion coefficient D is estimated from the Stokes-Einstein relation of $D = k_B T/\gamma$, where k_B is the Boltzmann constant and T the absolute temperature, and the lateral viscous drag γ is given by:

$$\gamma = 4\pi(\eta_1 + \eta_2)aC(\varepsilon)$$

where η_1 and η_2 are the dynamic viscosity values either side of the membrane, which we assume here are approximately the same at η_c the cytoplasmic viscosity. C is a function of $\varepsilon = 2a\eta_c/h\eta_m$ where η_m is the dynamic viscosity in the membrane itself. Since η_m is typically 2-3 orders of magnitude larger than η_c [39] then ε is sufficiently small to use an approximation for C of:

$$C \approx 1/(\varepsilon \ln(2/\varepsilon))$$

We used these formulations to generate a look-up table between D and a for the vegetative cell membrane in the mother cell, assuming $\eta_m \approx 600$ cP, and the emerging forespore cell membrane, assuming $\eta_m \approx 1{,}000$ cP, assuming $\eta_c \approx 1$ cP throughout (Fig. 5C) [40]. We estimated a consensus value for D in the mother cell from the population of unweighted mean D values determined from all cell stages I-III (Table S2) of 1.05 ± 0.06 μ^2m/s (±SEM, number of stages n = 5). We similarly estimated a consensus D value for the low mobility

sporulation stages II_i and II_{iii} of 0.47 ± 0.04 μ^2m/s (number of stages n = 2) and a consensus *D* value for the high mobility sporulation stages II_{ii} and III of 0.76 ± 0.05 μ^2m/s (number of stages n = 2). We then extrapolated these consensus values and SEM error estimates using the vegetative and forespore cell membrane look-up tables to determine corresponding mean values and ±SEM ranges for *a*.

2.8 Stoichiometry *vs.* localization

To compare foci stoichiometry as a function of location in the forespore, a simplified, normalised 1D coordinate was used. This was based on the generous forespore segmentation which extends from the mother cell side of the septa through to the outer edge of the cell pole. There was also significant variation in the size of this segmentation between cells. Thus a normalised coordinate was used, 0-1 from the two most extreme points of the forespore. This implied that on average both the septa and cell poles lie within the most extreme points of the predicted cell outline segmentation.

2.9 Structural and bioinformatics analysis

CCP4mg was used to render images of structures with PDB IDs: 5MQH SpoIIE(590-827) and 5UCG SpoIIE(457-827).[41]

2.10 Statistics and goodness of fit

Where means are presented and compared, students t-tests were run and p-values presented. For data-driven models, such as the stoichiometry modelling, χ^2 and p values are presented. For physical models such as FRAP and stokes fitting, the 95% confidence intervals on the fit parameters are presented as goodness of fit.

3. Results

3.1 Sporulation stage can be categorized using an accurate, high-throughput automated algorithm

We generated a chromosomally encoded fusion of SpoIIE to monomeric yellow fluorescent protein mYPet (a bright fluorescent protein with very short maturation time,<10 min[42] compared to >2hrs sporulation time, whose long excitation wavelength results in minimal contamination of cellular autofluorescence[43]) to report on SpoIIE localization (Table S1). We prepared cells for sporulation using nutrient-depleted media, incubating with the red lipophilic dye FM4-64 for visualizing *B. subtilis* membrane structures[44]. This allowed us to observe steady-state patterns of SpoIIE-mYPet and FM4-64 localization for sporulation stages I, II (with associated sub-stages) and III with single-molecule detection sensitivity via Slimfield (Fig. 1C), as well as standard epifluorescence microscopy (Fig. 1D,E and S1). We developed an automated high-throughput analysis framework using morphological transformations[33,45] on SpoIIE-mYPet and FM4-64 data, enabling us to categorize each cell into one of five different sporulation stages (I/pre-divisional, forespore formation stages II_i, II_{ii} and II_{iii}, and III after engulfment), validated by simulation and principal component analysis (Fig. 1F,G, Fig. S1). Our algorithm segments the SpoIIE and FM4-64 images to identify septa and forespore features and categorises them into appropriate stages but does not distinguish between E-ring structures in stage I[46,47] and SpoIIE localization in the septa in stage II_i. The measured proportions of cells in each stage (Fig. 1G) were qualitatively similar to those reported using manual, low-throughput methods[48]. Imaging a SpoIIE-mYPet strain including a *ΔspoIIQ* deletion (Table S1), defective in spore formation and unable to progress beyond stage II_{ii}, yielded similar relative proportions of cells in stages I, II_i and II_{ii} (Fig. S1). Although imperfect, resulting in some mis-characterisation (Fig. S1), our software is objective and enables study of cells which are not easily categorised by eye and avoids biasing our study to just previously accepted morphological features of sporulation.

3.2 SpoIIE is concentrated in the forespore, probably through equipartitioning

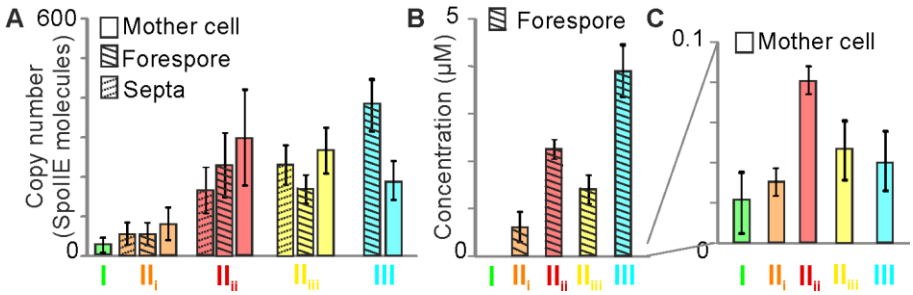

Figure 2: SpoIIE copy number (A) Mean and SEM SpoIIE copy number in mother cell, forespore and septa at each stage. (B) Concentration in the forespore, excluding the septa, at each stage. (C) Concentration in the mother cell, excluding the septa at each stage. Stage I (green),II_i (orange), II_{ii} (red), II_{iii} (yellow) and III (cyan). Mother cell copy numbers statistically higher than stage I by stage II_{ii} ($p=0.02$) and forespore copy number increases significantly between stage II_i and II_{ii} ($p=0.007$).

Slimfield images revealed distinct foci, as well as a more diffuse pool of fluorescent SpoIIE localized close to the cell membrane as expected (Movies S1-3). Slimfield employs a high numerical aperture objective lens with a high depth of field, thus a significant amount of fluorescence and even foci were detected in the middle of the cell. To check that this signal was really from membrane bound SpoIIE, we simulated images of membrane bound fluorophores in model *Bacillus* shaped cells and found similar patterns of localization (Fig. S1B). We used bespoke single particle localization[49] on the Slimfield data to track foci whose width was consistent with the measured point spread function (PSF) of our microscope, ~250nm. Foci could be tracked over consecutive images up to ~0.3s using rapid 5ms per frame sampling to a spatial precision of 40nm[27]. Tracking of distinct foci was coupled to molecular stoichiometry analysis by estimating the initial foci brightness and dividing this by the brightness of a single mYPet molecule[22,24,31,50,51] (Fig. S2A-C). We also observed a more diffuse pool of mYPet fluorescence, not detected as foci or caused by

436 cell autofluorescence which was negligible. Slimfield images were taken at the approximate
437 cell mid-body so foci at the top or bottom of the cell membrane are outside the depth of field,
438 generating the more diffuse fluorescence observed. By using integrated pixel intensities[27],
439 we determined the total SpoIIE copy number for each cell. Utilizing our stage categorization
440 algorithm we assigned each cell to one of the sporulation stages I-III, and also sub-divided
441 each into three sub-regions – a septum contributed by both mother cell and forespore, a
442 mother cell which excluded the septum, and a forespore which excluded the septum. We then
443 quantified the number of SpoIIE molecules specifically associated with each of these sub-
444 regions for each cell imaged (Fig. 2A, S2D).

445 These analyses (Table S2) show that the total SpoIIE copy number starts at a few tens
446 of molecules per cell in stage I, increasing as sporulation progresses to ~200 SpoIIE in
447 stage II_i, then rising to 700-800 molecules per cell in stages II_{ii} and II_{iii}, before dropping down
448 to ~580 molecules per cell in stage III after spore engulfment. The mother cell sub-region
449 excluding the septum reflects this trend, increasing SpoIIE copy number from
450 20-80 molecules between stages I-II_i, peaking at ~300 molecules in stages II_{ii}-II_{iii}, then tailing
451 off to ~190 molecules in stage III. Copy number in the septum and forespore also increases
452 throughout sporulation, starting at ~60 copies of SpoIIE at stage II_i increasing to ~400 copies
453 by stage III.

454 A key question is whether the SpoIIE concentration is higher in the forespore than the
455 mother cell, providing an explanation for cell-specific σ^F activation[19]. Our results support
456 this hypothesis, although they are complicated by ambiguity in septal fluorescence, which has
457 potential contributions from both the mother cell and the forespore, since the standard optical
458 resolution limit is greater than the pixel-level precision of image segmentation algorithms.
459 Even excluding the septal region, the forespore concentration of SpoIIE is an order of
460 magnitude higher than that in the mother cell (Fig 2B and C). This increased concentration

would arise from equipartitioning of SpoIIE between the mother cell and forespore combined with the ~6 times smaller volume of the forespore. We use volume as the simplest model here but similar results are obtained using the ~3 times smaller surface area also to account for SpoIIE being membrane bound. Intriguingly, arbitrarily attributing the septal fluorescence equally to the mother cell and forespore, the simplest model considering the ambiguity in which side it is on, results in approximately equal copy numbers in the two. It has been shown with an *in vitro* reconstituted system that a ~10-fold increase in the phosphatase activity of SpoIIE towards SpoIIAA~P is sufficient to release 90 % of σ^F from its inhibitory complex[52]. However, this imbalance in SpoIIE concentration cannot be immediately decisive *in vivo* as σ^F activation is delayed until stage II_{ii}. This suggests that following septation either SpoIIE is not immediately active as a phosphatase, or that following its dephosphorylation by SpoIIE, SpoIIAA is delayed in its capacity to displace σ^F from its inhibitory complex with the anti-sigma factor.

3.3 SpoIIE is a tetramer whose quaternary organization depends on spatial and temporal localization

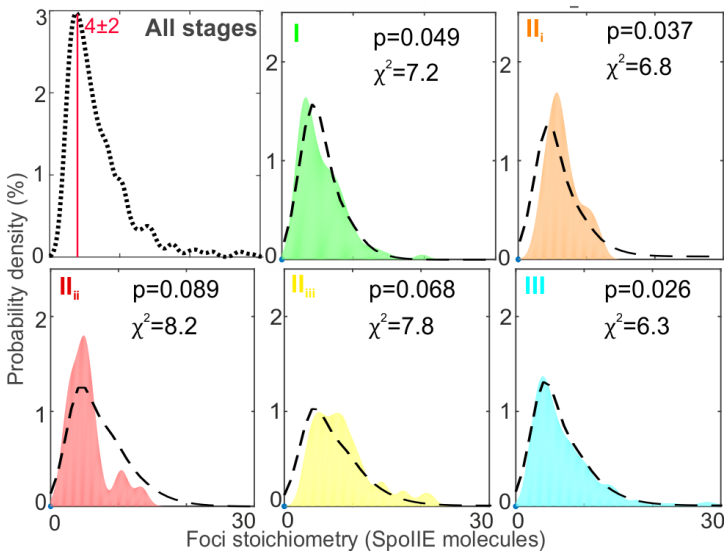

Figure 3: Stoichiometry of SpoIIE in the mother cell. Kernel density estimation (KDE) of the stoichiometry (i.e. number of SpoIIE molecules per detected fluorescent focus) in mother cell with predicted overlap tetramer model (black dotted line).Chi-squared χ^2 and probability of confidence p values indicated. Stage I (green),II_i (orange), II_{ii} (red), II_{iii} (yellow) and III (cyan).

Next, we sought to characterize the molecular architecture of functional SpoIIE by measuring the stoichiometry of fluorescent foci. In the mother cell, the apparent stoichiometry of tracked foci ranged from as few as two up to several tens of molecules, but with a clear peak at 4±2 SpoIIE molecules, conserved throughout stages I-III (Fig. 3). Using a randomized Poisson model for nearest-neighbour foci distances, whose key parameters comprise SpoIIE copy number and foci density, we calculated the probability of foci being separated by less than the optical resolution limit (thus detected as single foci of higher apparent stoichiometry) to be 20-40% in the mother cell. Overlap models which used the raw SpoIIE-mYPet intensity distribution (Fig S2C) in monomers, dimers, hexamers or octamers do not account for the observed stoichiometry distribution (Fig. S3). By contrast, we find that a tetramer overlap model generates reasonable agreement within experimental error for stages I-III in the mother cell (Fig. 3, dashed lines) for all stages, with a corresponding mean probability of confidence value of $p = 0.05$. Thus, we believe the most likely model among those trialled is that SpoIIE in the mother cell comprises predominantly tetramers.

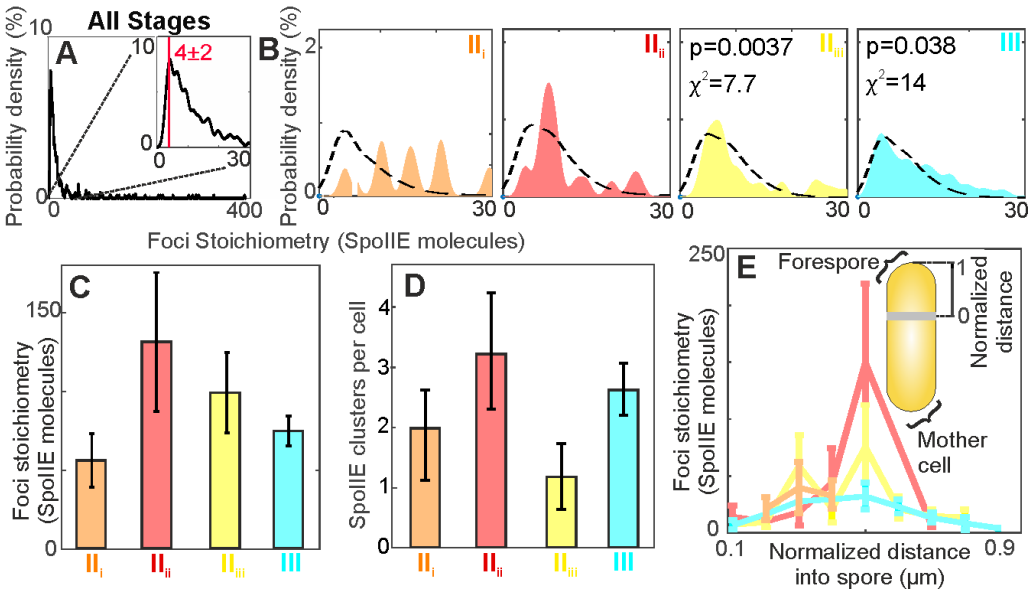

498

499 **Figure 4:** Stoichiometry of SpoIIE in the forespore. (A) Kernel density estimate (KDE) of
500 forespore stoichiometry pooled for all data, and zoom-in (inset), (B) in separate stages with
501 overlap tetramer model (black dotted line). (C) Bar chart of mean foci stoichiometry for foci
502 which have >20 molecules. Stage II_{ii} statistically higher than II_i (p=0.007) (D) Mean number
503 of foci detected per forespore. (E) Mean foci stoichiometry *vs.* normalised distance into spore
504 for each stage, (inset) schematic of forespore distance normalization. Stage I (green),II_i
505 (orange), II_{ii} (red), II_{iii} (yellow) and III (cyan).

506 For SpoIIE foci in the forespore or the septum, we find the same tetramer peak in the
507 measured stoichiometry distribution but with a longer tail of higher stoichiometry clusters
508 extending up to hundreds of SpoIIE molecules per focus (Fig. 4A, B). We adapted the
509 overlap model to account for different sizes and shapes of sporulation features at each stage
510 resulting in differences in the density of SpoIIE foci (Fig. 4B). The overlapping tetramer
511 model accounts only for low apparent stoichiometries near the tetramer peak and only in
512 stages II_{iii} and III. More generally, accounting for the apparent stoichiometry in the forespore
513 requires populations of higher order oligomeric SpoIIE clusters in the model fit, in addition to
514 tetramers. Excluding free tetrameric foci, we observe 1-3 clusters per cell (Fig. 4D) with the

515 mean cluster stoichiometry peaking in stage II_{ii} at >100 molecules per focus (Fig 4C) before
516 decreasing as the proportion of free tetramers increases again in stage III (Fig, S5A, B). We
517 find for foci present in the forespore the measured stoichiometry in all stages was periodic,
518 with a characteristic interval spacing of ~4 molecules (Fig. S4), suggesting that higher order
519 clusters are composed of associating SpoIIE tetramers.

520 Aspects of these *in vivo* observations are consistent with previous *in vitro* experiments.
521 Analytical ultracentrifugation experiments using a soluble fragment of SpoIIE, in which the
522 N-terminal 319 residues, which includes the 10 putative transmembrane segments, were
523 truncated, suggested that SpoIIE(319-872) formed hexamers and larger assemblies composed
524 of multiples of hexamers. [20] A more recent study of a similarly truncated protein
525 SpoIIE(325-872) fragment fused to maltose binding protein demonstrated reversible
526 manganese-dependent oligomerisation as evidenced by changes in sedimentation behaviour
527 and the observation of extended structures (50 nm x 10 nm) using electron microscopy[53] ,
528 although these authors did not speculate on the oligomeric state of the species involved.
529 Fragments of SpoIIE are challenging to express and purify (see also Lucet et al., 2000[12])
530 and their behaviour is sensitive to the size of the truncation. It is therefore not surprising that
531 the full length protein present in the membranes of living cells assembles in a different
532 manner. Whether SpoIIE forms oligomers *in vivo* in the absence of manganese would be an
533 interesting topic of further study.

534 We also observed that the stoichiometry of foci in the forespore was influenced by
535 their distance from the septum. We normalized the distance parallel to the long axis of each
536 cell from the mother cell side of the asymmetric septum through to the distal outer edge of
537 the cell containing the smaller forespore cell for all tracked foci and plotted this distance
538 against foci stoichiometry (Fig. 4E and S5C)., For stage II_i, foci are localized to the septum,
539 within ~300 nm , however, other stages contain foci which are delocalized over the full

extent of the emerging forespore (Fig. 4E); we find that the mean SpoIIE stoichiometry for these foci increases from ~12 to 150 molecules per focus (a factor of ~12) for stage II_{ii}. This observation supports the recently proposed mechanism for σ^F activation regulation[20] through clustering of SpoIIE in the direction of the pole at stage II_{ii}

3.4 SpoIIE foci mobility suggests that large multi-protein assemblies are present in stages II_i and II_{iii}

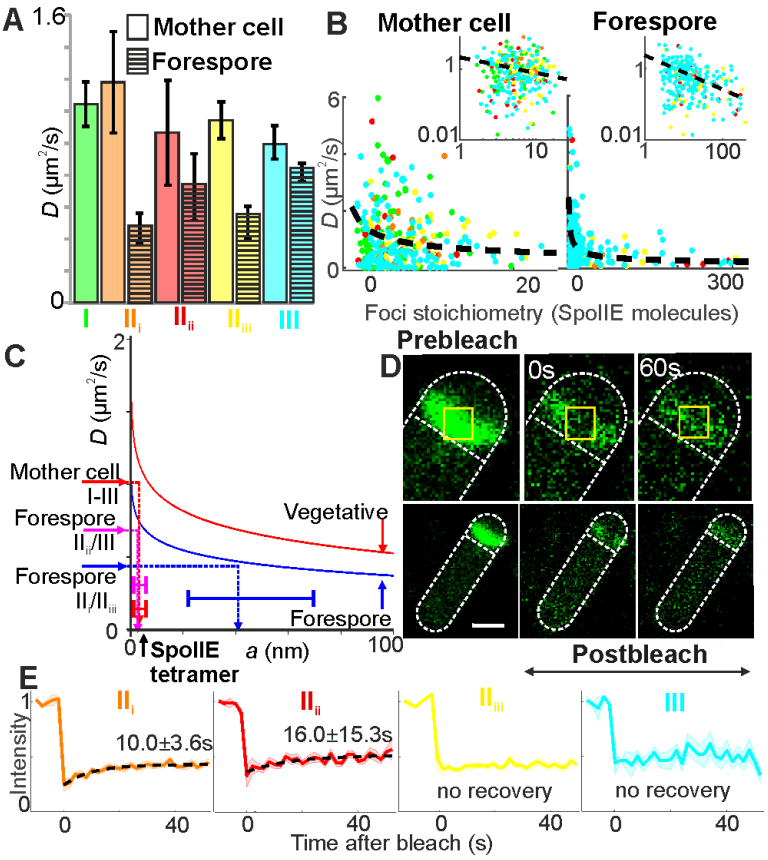

Figure 5: SpoIIE mobility (A) Bar chart of mean *D* for each compartment and stage, SEM errors. Forespore statistically different to mother cell in stages II_i and II_{iii} (p=0.018, 0.284, 0.004, 0.160, respectively for each stage. No significant change between each stage in the forespore , except III, p=0.003). (B) Scatter plots of stoichiometry *vs. D* for all stages in mother cell and forespore, log-log axes inset (power law model black line). (C) Variation of *D* with effective cluster cylinder radius *a* from frictional drag model, vegetative (i.e. as opposed to sporulating, shown in red) and forespore (blue) indicated with interpolations from *D* to *a* made from mother cell (all stages), and forespore stages (II_i/II_{iii}) and (II_{ii}/III), SEM errors. (D) FRAP from representative cell in stage II_i, immediately pre/post-bleach, and ~60s post-bleach, bleached region indicated (yellow squares). (E) Mean normalised fluorescence recovery for each stage, SEM bounds shown (shading). Dotted lines show best exponential fit

where recovery was detected, t_r and 95% confidence intervals indicated. Stage I (green),II_i (orange), II_{ii} (red), II_{iii} (yellow) and III (cyan). N=10-20 cells per stage.

We sought to determine the composition and function of clusters by analyzing their mobility in live cells. We find that SpoIIE fluorescent foci mobility in general was consistent with Brownian (i.e. normal) diffusion over short timescales irrespective of cell compartment or stage (Fig. S6, S7). In the mother cell, the mean value of the microscopic diffusion coefficient *D* was 0.9-1.2$\mu m^2/s$ while that in the forespore was lower by a factor of ~2 (Fig. 5A, Fig. S7 and Table S2). At the onset of sporulation in stage II_i foci mobility in the forespore is at its lowest with a mean *D* of 0.43±0.08$\mu m^2/s$, which increases during stage II_{ii} to 0.67±0.19$\mu m^2/s$, then decreases in stage II_{iii} to 0.50±0.09$\mu m^2/s$ before increasing again in stage III to 0.76±0.05$\mu m^2/s$, although only statistically significant in stage III. For stages I-III, *D* shows a dependence on stoichiometry *S*, indicating a trend for decreasing *D* with increasing SpoIIE content (Fig. 5B). Modelling this dependence as $D \sim S^{\alpha}$ indicates a power-law exponent α of 0.48 ± 0.18, with no measurable difference within error for each stage (Fig. S7).

Calculations of frictional drag on SpoIIE foci, using a consensus value for *D* from stages I-III for the mother cell, indicate an average Stokes radius (the radius of equivalent cylinder in the membrane) in the range 3-8nm (Fig. 5C, red dashed line). The N-terminal 330 residues of SpoIIE are predicted to form a membrane binding domain with 10 transmembrane α-helices[54]. A close packed circular arrangement of these helices, each with a diameter of 1.2 nm, would produce a SpoIIE tetramer comprising 40 transmembrane helices with a ~4 nm radius, consistent with our experimentally-derived estimate. By contrast, a ‘mean’ ~50-mer SpoIIE cluster has a Stokes radius of ~13nm. Thus the Stokes radius provides an estimate for

584 the real size of the diffusing SpoIIE complex, including any other protein partners diffusing
585 along with it.

586 For the forespore, the mean value *D* for higher SpoIIE mobility stages II_{ii} and III
587 indicates a range for Stokes radius consistent with clusters composed solely of SpoIIE
588 tetramers (Fig. 5C, magenta dashed line). However, the low SpoIIE mobility stages II_i and
589 II_{iii} indicate a Stokes radius approximately an order of magnitude higher at ~40 nm (Fig. 5C,
590 blue dashed line), far more than expected for a cluster of only 100 SpoIIE molecules. This
591 observation supports a model in which SpoIIE interacts with other proteins or complexes,
592 with these other unlabeled proteins here forming ~5x the SpoIIE foci surface area in the
593 membrane, increasing the apparent Stoke's radius. In stage II_i interactions would be with
594 components of the divisome[12–14] while in stage II_{iii} they would be with SpoIIQ, the
595 forespore component of an intercellular channel formed with proteins encoded on the *spoIIIA*
596 operon expressed in the mother cell[15]. In stage II_{ii} we find clusters of SpoIIE are likely not
597 associated with a protein partner as the Stokes radius is consistent only with the SpoIIE
598 present. This finding is also consistent with σ^F activation regulation[20].

599

600 **3.5 Forespore SpoIIE turnover depends on sporulation stage**

601 Using confocal microscopy of a similar cell strain but using monomeric GFP labelled
602 SpoIIE (i.e. SpoIIE-mGFP) we performed fluorescence recovery after photobleaching
603 (FRAP) experiments to photobleach the asymmetric septum at different stages and monitor
604 any subsequent fluorescence recovery (Fig. 5D). During stages II_i and II_{ii} there is a relatively
605 slow recovery with mean exponential recovery time t_r of 10±3.6s and 16.0±15.3s respectively
606 (Fig. 5E, S7). Our finding that t_r is not directly correlated to *D* in each stage suggests that
607 turnover here is reaction- as opposed to diffusion-limited; it may be limited by an effective

608 off-rate as observed in other complex bacterial structures such as components of the flagellar
609 motor or replisome[55,56]. In subsequent stages II_{iii} and III, no recovery is detectable within
610 error, though lower levels of fluorescence and numbers of cells in stage III result in higher
611 measurement noise which limits the sensitivity for detecting low levels of putative recovery.

612 Divisome components such as FtsZ have been shown to turnover in similar FRAP
613 studies[57], consistent with our stage II_i findings when SpoIIE associates with the divisome.
614 Turnover is also expected at stage II_{ii} when SpoIIE is released. At stage II_{iii} SpoIIE interacts
615 with the SpoIIQ-SpoIIIAH channel which may account for the lack of turnover. A similar
616 absence is unexpected at stage III when SpoIIE is released and has no known function. This
617 suggests that at stage III, SpoIIE is released quickly then anchored into the spore, or that the
618 viscosity in spore itself has changed as has been shown to occur during sporulation[40].

619

620

4. Discussion

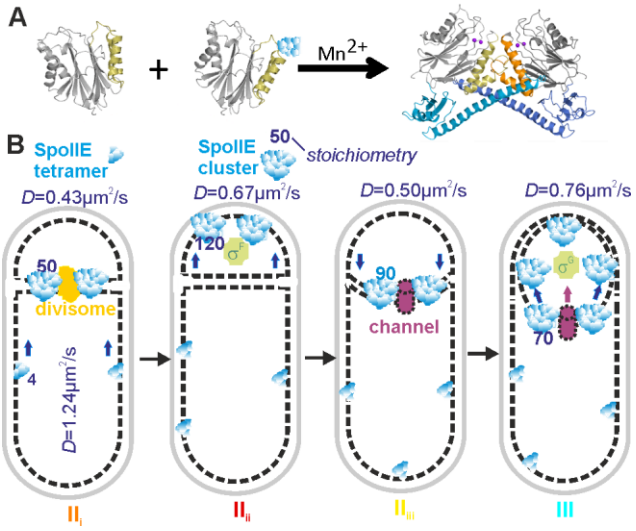

Figure 6: Model of SpoIIE dynamics during sporulation. (A) Activation of phosphatase involves dimerization, and recruitment of Mn^{2+} ions. Isolated phosphatase, SpoIIE(590-827) (PDB: 5MQH), is monomeric while a longer fragment, SpoIIE(457-827) (PDB: 5UCG), forms dimers about an interface dominated by a long helix spanning residues 473-518. Subunits in dimer distinguished by shading: PP2C domains (gray), switch helices (orange), regulatory domains (blue), Mn^{2+} ions (purple spheres, modeled onto structure following superposition of PstP structure from *M. tuberculosis* PDB: 1TXO). (B) Schematic of SpoIIE architecture and *D* at each stage: SpoIIE tetramers (blue), divisome (yellow), activated sigma factors (green), and SpoIIQ channel (purple) shown. Arrows indicate SpoIIE's release or re-capture to the septa.

SpoIIE performs multiple important functions. For example, it is essential to form a proper sporulation septum as well as to activate SigF. Without SpoIIE no spore can be formed and also there are many point mutations characterized in *spoIIE* which cause complete arrest of cell differentiation. However, how it switches roles at different stages has been unclear. It is not known how SpoIIE localizes to the polar septum, how it causes FtsZ to relocalize from mid-cell to one of the cell poles, what role it plays in septal thinning, or how

its SpoIIAA-P phosphatase activity is controlled so that σ^F activation is delayed until the asymmetric septum is completed[7,11]. How SpoIIE brings about forespore-specific activation of σ^F is a subject of particular interest[58]. Plausible suggested mechanisms include preferential SpoIIE localization on the forespore face of the septum[59], transient gene asymmetry leading to accumulation of a SpoIIE inhibitor in the mother cell[58], and the volume difference between compartments leading to higher specific activity of equipartitioned SpoIIE[60,61]. Most recently, it was shown that mother cell restricted intracellular proteolysis of SpoIIE by the membrane bound protease FtsH is important for compartment-specific activation of σ^F[20]. Our findings indicate that SpoIIE operates as an oligomer whose stoichiometry and mobility switch in the forespore according to specific sporulation stage, driving morphological changes, as opposed to changes being primarily dependent on the differential effective concentration of SpoIIE in either mother cell or forespore. In particular, complexes comprising four SpoIIE molecules predominate in the mother cell and at multiple stages in the forespore. Crucially, we observe reversible assembly of these tetrameric SpoIIE entities into higher order multimers during stage II_{ii} when the protein localizes towards the pole and its latent protein phosphatase activity is manifested.

Unlike previous microscopy of YFP-labelled SpoIIE which suggested a pattern of localization almost exclusively in the forespore following asymmetric septation[20], our higher sensitivity shows SpoIIE content is at most 10-30% greater in the early forespore and septum compared to the mother cell if all of the SpoIIE in the septum is assigned to the forespore. An equipartition of septal SpoIIE results in approximately equal copy number in the mother cell and forespore. However, the more than 6 times smaller forespore volume[19] results in a higher SpoIIE concentration by a factor of ~6-8, depending on partitioning of septal SpoIIE. It was shown previously that a 10-fold difference in SpoIIE phosphatase activity towards its substrate SpoIIAA~P could account for all-or-nothing compartmental

664 regulation of σ^F activity[62]. The bias towards higher copy number values in the forespore
665 aligns with the recent suggestion that SpoIIE captured at the forespore pole is protected
666 against proteolysis[20]. In this model, SpoIIE sequestered in the polar divisome, is handed-
667 off to the adjacent forespore pole following cytokinesis. This forespore polar SpoIIE is
668 protected from FtsH-mediated proteolysis by oligomerisation, which is clearly described by
669 our observations. Compartment specificity results from the proximity of the forespore pole to
670 the site of asymmetric division.

671 Crystallographic and biophysical studies reveal that SpoIIE(590-827), comprising the
672 phosphatase domain, is a monomer while SpoIIE(457-827), comprising the phosphatase plus
673 part of the upstream regulatory domain, is dimeric (Fig. 6A)[63,64]. Comparison of these
674 structures and mapping of mutational data onto them led to the proposal that PP2C domains
675 in SpoIIE(590-827) and SpoIIE(457-827) crystals represent inactive and active states
676 respectively. Activation is accompanied by a 45° rigid-body rotation of two 'switch'
677 helices[64]. This switch is set by a long α-helix in the regulatory domain which mediates
678 dimerization (Fig. 6A). Movement of the switch helices upon dimerization translates a
679 conserved glycine (Gly629 in SpoIIE) into the active site where it can participate in
680 cooperative binding to two catalytic manganese ions. These ions are conserved in PP2C
681 phosphatases and here would be expected to activate a water molecule for nucleophilic attack
682 at the phosphorus of the phosphorylated serine 57 residue in SpoIIAA-P. The increase in
683 SpoIIE stoichiometry observed upon activation *in vivo* is consistent with these structural
684 findings although clearly larger assemblies are implied. We can speculate on the basis of the
685 data presented here these larger assemblies arise from further homomeric quaternary
686 interactions mediated by the substantial membrane binding domain and/or the component of
687 the regulatory domain which has yet to be fully characterized. The results are consistent with
688 the hand-off model[20] in which release from the divisome allows SpoIIE tetramers to

diffuse away from the septum and self-associate to form high stoichiometry clusters in a spontaneous process with similarities to that observed for the plasmalemmal protein syntaxin[65]. We speculate that the free energy of reassembly is used to flip the helical switch, allowing manganese acquisition and activation of phosphatase activity.

Changes in oligomeric state and quaternary organization of proteins are widespread mechanisms for regulating biological activity. These can be induced variously by binding of allosteric ligands, covalent modification, proteolytic processing and reversible interactions with protein agonists or antagonists. SpoIIE, which transitions between complexes which are unusually large, is transiently active as a phosphatase after its release from an inhibitory complex with the divisome. Regulation of phosphatase activity through sequestration is also seen in adaptation to drought in plants; the phosphatase HAB1 dephosphorylates the kinase SnRK2, inhibiting transcription of drought tolerance genes until the complex of the hormone, abscisic acid and its receptor, PYR, binds to and inhibits the phosphatase HAB1[66].

Our findings show more generally that we can combine robust cell categorization with single-molecule microscopy and quantitative copy number and stoichiometry analysis to follow complex morphologies during differentiation (Fig. 6B). Importantly, these tools provide new insight into the role of SpoIIE by monitoring its molecular composition and spatiotemporal dynamics, linking together different stages of cell development. Our findings show that the function of a key regulatory protein can be altered depending upon its state of multimerization and mobility, enabling different roles at different cell stages. Future applications of these methods may involve multicolor observations of SpoIIE with other interaction partners at different sporulation stages. Optimising these advanced imaging tools in the model Gram-positive *B. subtilis* may ultimately enable real time observations of more complex cellular development, paving the way for future studies of tissue morphogenesis in more challenging multicellular organisms. More generally our findings demonstrate that the

application of super-resolved single-molecule optical proteomics biotechnology can enable new mechanistic insight into complex cell stage dependent processes in single living cells which are technically too challenging to achieve using traditional methods. Such findings are made possible by a range of innovative computational tools to categorise cell cycle stage and to quantify single-particle tracks, and enable not only new understanding of the dynamic patterns of spatial localization of a key protein used in triggering cell development, but also in posing questions about its structural properties at different cell cycle stages.

Data availability. Data included in full in main text and supplementary files. Raw data available from authors.

Software access. Code written in MATLAB available from Sporulationanalyser at https://sourceforge.net/projects/york-biophysics/

Declaration of Interests The authors declare no conflict of interest.

Acknowledgments

Authors thank Niels Bradshaw and Adam Hughes for helpful comments. Supported by Royal Society, MRC (grant MR/K01580X/1), BBSRC (grant BB/N006453/1) to M.L. and grants 2/0007/17 from Slovak Academy of Sciences and Slovak Research and Development Agency (APVV-14-0181 and APVV-18-0104) to I.B. Part-funded by the Wellcome Trust [ref: 204829] through Centre for Future Health at the University of York to A.J.M.W.

References

[1] Errington J. From spores to antibiotics via the cell cycle. Microbiology 2010;156:1–13. https://doi.org/10.1099/mic.0.035634-0.

[2] Rudner DZ, Losick R. Morphological coupling in development: lessons from prokaryotes. Dev Cell 2001;1:733–42.

[3] McKenney PT, Eichenberger P. Dynamics of spore coat morphogenesis in Bacillus subtilis. Mol Microbiol 2012;83:245–60. https://doi.org/10.1111/j.1365-2958.2011.07936.x.

[4] Ben-Yehuda S, Losick R. Asymmetric cell division in B. subtilis involves a spiral-like

746 intermediate of the cytokinetic protein FtsZ. Cell 2002;109:257–66.
747 [5] Levin PA, Losick R, Stragier P, Arigoni F. Localization of the sporulation protein
748 SpoIIE in Bacillus subtilis is dependent upon the cell division protein FtsZ. Mol
749 Microbiol 1997;25:839–46. https://doi.org/10.1111/j.1365-2958.1997.mmi505.x.
750 [6] Pogliano J, Osborne N, Sharp MD, Mello AA De, Perez A, Sun YL, et al. A vital stain
751 for studying membrane dynamics in bacteria: A novel mechanism controlling septation
752 during Bacillus subtilis sporulation. Mol Microbiol 1999;31:1149–59.
753 https://doi.org/10.1046/j.1365-2958.1999.01255.x.
754 [7] Barák I, Youngman P. SpoIIE mutants of Bacillus subtilis comprise two distinct
755 phenotypic classes consistent with a dual functional role for the SpoIIE protein. J
756 Bacteriol 1996;178:4984–9.
757 [8] Feucht A, Magnin T, Yudkin MD, Errington J. Bifunctional protein requried for
758 asymmetric cell division and cell-specific transcription in Bacillus subtilis. Genes Dev
759 1996;10:794–803. https://doi.org/10.1101/gad.10.7.794.
760 [9] Losick R, Stragier P. Crisscross regulation of cell-type-specific gene expression during
761 development in B. subtilis. Nature 1992;355:601–4. https://doi.org/10.1038/355601a0.
762 [10] Arigoni F, Pogliano K, Webb CD, Stragier P, Losick R. Localization of protein
763 implicated in establishment of cell type to sites of asymmetric division. Science
764 1995;270:637–40.
765 [11] King N, Dreesen O, Stragier P, Pogliano K, Losick R. Septation, dephosphorylation,
766 and the activation of sigmaF during sporulation in Bacillus subtilis. Genes Dev
767 1999;13:1156–67.
768 [12] Lucet I, Feucht A, Yudkin MD, Errington J. Direct interaction between the cell
769 division protein FtsZ and the cell differentiation protein SpoIIE. EMBO J
770 2000;19:1467–75. https://doi.org/10.1093/emboj/19.7.1467.

771 [13] Muchová K, Chromiková Z, Bradshaw N, Wilkinson AJ, Barák I. Morphogenic
772 Protein RodZ Interacts with Sporulation Specific SpoIIE in Bacillus subtilis. PLoS
773 One 2016;11:e0159076. https://doi.org/10.1371/journal.pone.0159076.
774 [14] Eswaramoorthy P, Winter PW, Wawrzusin P, York AG, Shroff H, Ramamurthi KS.
775 Asymmetric division and differential gene expression during a bacterial developmental
776 program requires DivIVA. PLoS Genet 2014;10:e1004526.
777 https://doi.org/10.1371/journal.pgen.1004526.
778 [15] Campo N, Marquis KA, Rudner DZ. SpoIIQ anchors membrane proteins on both sides
779 of the sporulation septum in Bacillus subtilis. J Biol Chem 2008;283:4975–82.
780 https://doi.org/10.1074/jbc.M708024200.
781 [16] Meisner J, Wang X, Serrano M, Henriques AO, Moran CP. A channel connecting the
782 mother cell and forespore during bacterial endospore formation. Proc Natl Acad Sci U
783 S A 2008;105:15100–5. https://doi.org/10.1073/pnas.0806301105.
784 [17] Doan T, Morlot C, Meisner J, Serrano M, Henriques AO, Moran CP, et al. Novel
785 secretion apparatus maintains spore integrity and developmental gene expression in
786 Bacillus subtilis. PLoS Genet 2009;5. https://doi.org/10.1371/journal.pgen.1000566.
787 [18] Camp AH, Losick R. factor during sporulation in Bacillus subtilis A feeding tube
788 model for activation of a cell-specific transcription factor during sporulation in
789 Bacillus subtilis. Genes Dev 2009:1014–24. https://doi.org/10.1101/gad.1781709.
790 [19] Barák I, Muchová K. The positioning of the asymmetric septum during sporulation in
791 Bacillus subtilis. PLoS One 2018;13:e0201979.
792 https://doi.org/10.1371/journal.pone.0201979.
793 [20] Bradshaw N, Losick R. Asymmetric division triggers cell-specific gene expression
794 through coupled capture and stabilization of a phosphatase. Elife 2015;4:1–18.
795 https://doi.org/10.7554/eLife.08145.

[21] Plank M, Wadhams GH, Leake MC. Millisecond timescale slimfield imaging and automated quantification of single fluorescent protein molecules for use in probing complex biological processes. Integr Biol (Camb) 2009;1:602–12. https://doi.org/10.1039/b907837a.

[22] Reyes-Lamothe R, Sherratt DJ, Leake MC. Stoichiometry and architecture of active DNA replication machinery in Escherichia coli. Science 2010;328:498–501. https://doi.org/10.1126/science.1185757.

[23] Badrinarayanan A, Reyes-Lamothe R, Uphoff S, Leake MC, Sherratt DJ. In vivo architecture and action of bacterial structural maintenance of chromosome proteins. Science 2012;338:528–31. https://doi.org/10.1126/science.1227126.

[24] Leake MC, Chandler JH, Wadhams GH, Bai F, Berry RM, Armitage JP. Stoichiometry and turnover in single, functioning membrane protein complexes. Nature 2006;443:355–8. https://doi.org/10.1038/nature05135.

[25] Harwood CR. Molecular biological methods for Bacillus. Chichester ;;New York: Wiley; 1990.

[26] Lewis PJ, Marston AL. GFP vectors for controlled expression and dual labelling of protein fusions in Bacillus subtilis. Gene 1999;227:101–9. https://doi.org/10.1016/S0378-1119(98)00580-0.

[27] Wollman AJM, Leake MC. Millisecond single-molecule localization microscopy combined with convolution analysis and automated image segmentation to determine protein concentrations in complexly structured, functional cells, one cell at a time. Faraday Discuss 2015;184:401–24. https://doi.org/10.1039/c5fd00077g.

[28] Stracy M, Lesterlin C, Garza de Leon F, Uphoff S, Zawadzki P, Kapanidis AN. Live-cell superresolution microscopy reveals the organization of RNA polymerase in the bacterial nucleoid. Proc Natl Acad Sci U S A 2015;112:E4390-9.

https://doi.org/10.1073/pnas.1507592112.

[29] Kusumi A, Sako Y, Yamamoto M. Confined lateral diffusion of membrane receptors as studied by single particle tracking (nanovid microscopy). Effects of calcium-induced differentiation in cultured epithelial cells. Biophys J 1993;65:2021–40. https://doi.org/10.1016/S0006-3495(93)81253-0.

[30] Leake MC, Grützner A, Krüger M, Linke WA. Mechanical properties of cardiac titin's N2B-region by single-molecule atomic force spectroscopy. J Struct Biol 2006;155:263–72. https://doi.org/10.1016/j.jsb.2006.02.017.

[31] Wollman AJ, Shashkova S, Hedlund EG, Friemann R, Hohmann S, Leake MC. Transcription factor clusters regulate genes in eukaryotic cells. Elife 2017;6. https://doi.org/10.7554/eLife.27451.

[32] Michalet X. Mean square displacement analysis of single-particle trajectories with localization error: Brownian motion in an isotropic medium. Phys Rev E 2010;82:41914. https://doi.org/10.1103/PhysRevE.82.041914.

[33] Wollman AJM, Miller H, Foster S, Leake MC. An automated image analysis framework for segmentation and division plane detection of single live Staphylococcus aureus cells which can operate at millisecond sampling time scales using bespoke Slimfield microscopy. Phys Biol 2016;13:55002. https://doi.org/10.1088/1478-3975/13/5/055002.

[34] Hotelling H. Analysis of a complex of statistical variables into principal components. J Educ Psychol 1933;24:417–41. https://doi.org/10.1037/h0071325.

[35] Weart RB, Lee AH, Chien A-C, Haeusser DP, Hill NS, Levin PA. A Metabolic Sensor Governing Cell Size in Bacteria. Cell 2007;130:335–47. https://doi.org/10.1016/j.cell.2007.05.043.

[36] Llorente-Garcia I, Lenn T, Erhardt H, Harriman OL, Liu L-N, Robson A, et al. Single-

molecule in vivo imaging of bacterial respiratory complexes indicates delocalized oxidative phosphorylation. Biochim Biophys Acta 2014;1837:811–24. https://doi.org/10.1016/j.bbabio.2014.01.020.

[37] Saffman PG, Delbrück M. Brownian motion in biological membranes. Proc Natl Acad Sci U S A 1975;72:3111–3.

[38] Hughes BD, Pailthorpe BA, White LR. The translational and rotational drag on a cylinder moving in a membrane. J Fluid Mech 1981;110:349. https://doi.org/10.1017/S0022112081000785.

[39] Fushimi K, Verkman AS. Low viscosity in the aqueous domain of cell cytoplasm measured by picosecond polarization microfluorimetry. J Cell Biol 1991;112:719–25. https://doi.org/10.1083/JCB.112.4.719.

[40] Loison P, Hosny NA, Gervais P, Champion D, Kuimova MK, Perrier-Cornet J-M. Direct investigation of viscosity of an atypical inner membrane of Bacillus spores: A molecular rotor/FLIM study. BBA - Biomembr 2013;1828:2436–43. https://doi.org/10.1016/j.bbamem.2013.06.028.

[41] McNicholas S, Potterton E, Wilson KS, Noble MEM. Presenting your structures: the CCP4mg molecular-graphics software. Acta Crystallogr D Biol Crystallogr 2011;67:386–94. https://doi.org/10.1107/S0907444911007281.

[42] Yarden Y, Sliwkowski MX. Untangling the ErbB signalling network. Nat Rev Mol Cell Biol 2001;2:127–37.

[43] Nguyen AW, Daugherty PS. Evolutionary optimization of fluorescent proteins for intracellular FRET. Nat Biotechnol 2005;23:355–60. https://doi.org/10.1038/nbt1066.

[44] Sharp MD, Pogliano K. An in vivo membrane fusion assay implicates SpoIIIE in the final stages of engulfment during Bacillus subtilis sporulation. Proc Natl Acad Sci U S A 1999;96:14553–8.

871 [45] Lund VA, Wacnik K, Turner RD, Cotterell BE, Walther CG, Fenn SJ, et al. Molecular
872 coordination of Staphylococcus aureus cell division. Elife 2018;7:e32057.
873 https://doi.org/10.7554/eLife.32057.
874 [46] Arigoni F, Pogliano K, Webb CD, Stragier P, Losick R. Localization of protein
875 implicated in establishment of cell type to sites of asymmetric division. Science (80-)
876 1995;270:637–40. https://doi.org/10.1126/science.270.5236.637.
877 [47] Wu LJ, Feucht A, Errington J. Prespore-specific gene expression in Bacillus subtilis is
878 driven by sequestration of SpoIIe phosphatase to the prespore side of the asymmetric
879 septum. Genes Dev 1998;12:1371–80. https://doi.org/10.1101/gad.12.9.1371.
880 [48] Hauser PM, Errington J. Characterization of cell cycle events during the onset of
881 sporulation in Bacillus subtilis. J Bacteriol 1995;177:3923–31.
882 [49] Miller H, Zhou Z, Wollman AJM, Leake MC. Superresolution imaging of single DNA
883 molecules using stochastic photoblinking of minor groove and intercalating dyes.
884 Methods 2015;88:81–8. https://doi.org/10.1016/j.ymeth.2015.01.010.
885 [50] Stracy M, Wollman AJM, Kaja E, Gapinski J, Lee J-E, Leek VA, et al. Single-
886 molecule imaging of DNA gyrase activity in living *Escherichia coli*. Nucleic Acids
887 Res 2019;47:210–20. https://doi.org/10.1093/nar/gky1143.
888 [51] Sun Y, Wollman AJM, Huang F, Leake MC, Liu L-N. Single-Organelle Quantification
889 Reveals Stoichiometric and Structural Variability of Carboxysomes Dependent on the
890 Environment. Plant Cell 2019;31:1648–64. https://doi.org/10.1105/tpc.18.00787.
891 [52] Clarkson J, Campbell ID, Yudkin MD. Efficient Regulation of σF, the First
892 Sporulation-specific Sigma Factor in B.subtilis. J Mol Biol 2004;342:1187–95.
893 https://doi.org/10.1016/j.jmb.2004.07.090.
894 [53] Król E, de Sousa Borges A, Kopacz M, Scheffers D-J. Metal-dependent SpoIIE
895 oligomerization stabilizes FtsZ during asymmetric division in Bacillus subtilis. PLoS

One 2017;12:e0174713. https://doi.org/10.1371/journal.pone.0174713.

[54] Arigoni F, Guérout-Fleury AM, Barák I, Stragier P. The SpoIIE phosphatase, the sporulation septum and the establishment of forespore-specific transcription in Bacillus subtilis: a reassessment. Mol Microbiol 1999;31:1407–15.

[55] Delalez NJ, Wadhams GH, Rosser G, Xue Q, Brown MT, Dobbie IM, et al. Signal-dependent turnover of the bacterial flagellar switch protein FliM. Proc Natl Acad Sci U S A 2010;107:11347–51. https://doi.org/10.1073/pnas.1000284107.

[56] Leake MC, Chandler JH, Wadhams GH, Bai F, Berry RM, Armitage JP. Stoichiometry and turnover in single, functioning membrane protein complexes. Nature 2006;443:355–8. https://doi.org/10.1038/nature05135.

[57] Arumugam S, Petrašek Z, Schwille P. MinCDE exploits the dynamic nature of FtsZ filaments for its spatial regulation. Proc Natl Acad Sci U S A 2014;111:E1192-200. https://doi.org/10.1073/pnas.1317764111.

[58] Barák I, Wilkinson AJ. Where asymmetry in gene expression originates. Mol Microbiol 2005;57:611–20. https://doi.org/10.1111/j.1365-2958.2005.04687.x.

[59] Guberman JM, Fay A, Dworkin J, Wingreen NS, Gitai Z. PSICIC: noise and asymmetry in bacterial division revealed by computational image analysis at sub-pixel resolution. PLoS Comput Biol 2008;4:e1000233. https://doi.org/10.1371/journal.pcbi.1000233.

[60] Iber D, Clarkson J, Yudkin MD, Campbell ID. The mechanism of cell differentiation in Bacillus subtilis. Nature 2006;441:371–4. https://doi.org/10.1038/nature04666.

[61] Igoshin OA, Price CW, Savageau MA. Signalling network with a bistable hysteretic switch controls developmental activation of the ??F transcription factor in Bacillus subtilis. Mol Microbiol 2006;61:165–84. https://doi.org/10.1111/j.1365-2958.2006.05212.x.

[62] Yudkin MD, Clarkson J. Differential gene expression in genetically identical sister cells: the initiation of sporulation in *Bacillus subtilis* †. Mol Microbiol 2005;56:578–89. https://doi.org/10.1111/j.1365-2958.2005.04594.x.

[63] Levdikov VM, Blagova E V., Rawlings AE, Jameson K, Tunaley J, Hart DJ, et al. Structure of the phosphatase domain of the cell fate determinant SpoIIE from Bacillus subtilis. J Mol Biol 2012;415:343–58. https://doi.org/10.1016/j.jmb.2011.11.017.

[64] Bradshaw N, Levdikov VM, Zimanyi CM, Gaudet R, Wilkinson AJ, Losick R. A widespread family of serine/threonine protein phosphatases shares a common regulatory switch with proteasomal proteases. Elife 2017;6. https://doi.org/10.7554/eLife.26111.

[65] Sieber JJ, Willig KI, Kutzner C, Gerding-Reimers C, Harke B, Donnert G, et al. Anatomy and Dynamics of a Supramolecular Membrane Protein Cluster. Science (80-) 2007;317:1072–6. https://doi.org/10.1126/science.1141727.

[66] Soon F-F, Ng L-M, Zhou XE, West GM, Kovach A, Tan MHE, et al. Molecular mimicry regulates ABA signaling by SnRK2 kinases and PP2C phosphatases. Science 2012;335:85–8. https://doi.org/10.1126/science.1215106.